

Analytic model for feature maps in the primary visual cortex

X. Liu^{1,2} and P.A. Robinson^{1,2}

¹School of Physics, University of Sydney, New South Wales 2006, Australia

²Center for Integrative Brain Function, University of Sydney, New South Wales 2006, Australia

January 6, 2022

Abstract

A compact analytic model is proposed to describe the combined orientation preference (OP) and ocular dominance (OD) features of simple cells and their layout in the primary visual cortex (V1). This model consists of three parts: (i) an anisotropic Laplacian (AL) operator that represents the local neural sensitivity to the orientation of visual inputs; (ii) a receptive field (RF) operator that models the anisotropic spatial RF that projects to a given V1 cell over scales of a few tenths of a millimeter and combines with the AL operator to give an overall OP operator; and (iii) a map that describes how the parameters of these operators vary approximately periodically across V1. The parameters of the proposed model maximize the neural response at a given OP with an OP tuning curve fitted to experimental results. It is found that the anisotropy of the AL operator does not significantly affect OP selectivity, which is dominated by the RF anisotropy, consistent with Hubel and Wiesel's original conclusions that orientation tuning width of V1 simple cell is inversely related to the elongation of its RF. A simplified OP-OD map is then constructed to describe the approximately periodic OP-OD structure of V1 in a compact form. Specifically, the map is approximated by retaining its dominant spatial Fourier coefficients, which are shown to suffice to reconstruct the overall structure of the OP-OD map. This representation is a suitable form to analyze observed maps compactly and to be used in neural field theory of V1. Application to independently simulated V1 structures shows that observed irregularities in the map correspond to a spread of dominant coefficients in a circle in Fourier space.

1 Introduction

V1 is the first cortical area that processes visual inputs from the lateral geniculate nucleus (LGN) of the thalamus before projecting output signals to higher visual areas (Miikkulainen et al., 2005). The feedforward visual pathway from the eyes to V1 involves two main processing steps: (i) light levels at a given spatial location are detected and converted into neural signals by the retina ganglion cells; and (ii) the neural signals are transmitted to V1 through the lateral geniculate nuclei (LGN) of the thalamus (Schiller and Tehovnik, 2015). LGN neurons have approximately circular receptive fields with either a central ON region (activity enhanced by light incident there) surrounded by an OFF annulus (activity suppressed by light incident there), or vice versa (DeAngelis et al., 1995; Hubel and Wiesel, 1961).

Similarly to other parts of the cortex, V1 can be approximated as a two-dimensional sheet when studying the spatial structure of the retinotopic map (Tovée, 1996). V1 neurons, which respond to same eye preference or orientation preference, are arranged in columns perpendicular to the cortical surface. Columns do not have sharp boundaries; rather, feature preferences gradually vary across the surface of

V1. These maps are overlaid such that a given neuron responds to several features (Hubel and Wiesel, 1962b, 1968, 1974a; Miikkulainen et al., 2005).

Two prominent feature preferences of V1 cells are their layout in a combined the OP-OD map, as seen in Fig. 1(a), which shows an example from experiment (Blasdel, 1992). Hubel and Wiesel (1968) found that neurons that respond preferentially to stimuli from one eye or the other are arranged in alternating bands across layer 4C of V1 in macaque monkeys, and these bands are termed left and right OD columns. The average OD column width in mammals ranges from $\sim 0.5 - 1$ mm (Adams et al., 2007; Horton and Adams, 2005). An OP column, sometimes called an iso-orientation slab, comprises neurons that respond to similar edge orientation in a visual field. Each OP column not only spans several cortical layers vertically, but also extends $25 - 50 \mu\text{m}$ laterally in monkey. Moreover, OP normally varies continuously as a function of the cortical position, covering the complete range 0° to 180° of edge orientations (Hubel and Wiesel, 1974a, 1977; Obermayer and Blasdel, 1993). Optical imaging reveals that OP columns are quasiperiodic, and are arranged as pinwheels, within which each of the OPs varies azimuthally around a center called a singularity (Blasdel, 1992; Bonhoeffer and Grinvald, 1991, 1993; Swindale, 1996). Furthermore, the OP in each pinwheel increases either clockwise (negative pinwheel) or counterclockwise (positive pinwheel) and most neighboring pinwheels have opposite signs (Götz, 1987, 1988). Examples of positive and negative OP pinwheels are outlined in Fig. 1(a). The superimposed OD and OP maps have specific relationships, including that: (i) most pinwheels are centered near the middle of OD stripes; (ii) linear zones, which are formed by near-parallel OP columns, usually connect two singularities and cross the border of OD stripes at right angles (Bartfeld and Grinvald, 1992), as highlighted in the white rectangle in Fig. 1(a). Additionally, various studies (Chklovskii and Koulakov, 2004; Koulakov and Chklovskii, 2001; Mitchison, 1991, 1995) have argued that the appearance of the OP-OD map reflects wiring optimization of local neuron connectivity, in which the distance between neurons with similar feature preference is kept as small as possible.

According to the quasiperiodicity of the feature preference of V1, previous studies (Bressloff and Cowan, 2002; Veltz et al., 2015) suggested that the functional maps of V1 can be approximated by a spatially periodic network of fundamental domains, each of which is called a hypercolumn. Each hypercolumn represents a small piece of V1, which consists of left and right OD stripes with a pair of positive and negative pinwheels in each, so as to ensure the complete coverage of the OP and OD selectivity.

Orientation selectivity plays a primary role in early-stage visual processing. One way to characterize the preferred orientations of a single neuron is to measure the tuning curve from its neuronal response to visual stimuli with various orientations. Figure 1(b) shows an experimental orientation tuning curve obtained from single unit responses in area 17 of adult cat, with optimal orientation angle of 90° (Swindale, 1998). A typical full width at half maximum (FWHM) of such a curve is $\sim 35^\circ$.

The mapping of inputs from the retina to V1 is organized in a retinotopic manner. Visual information

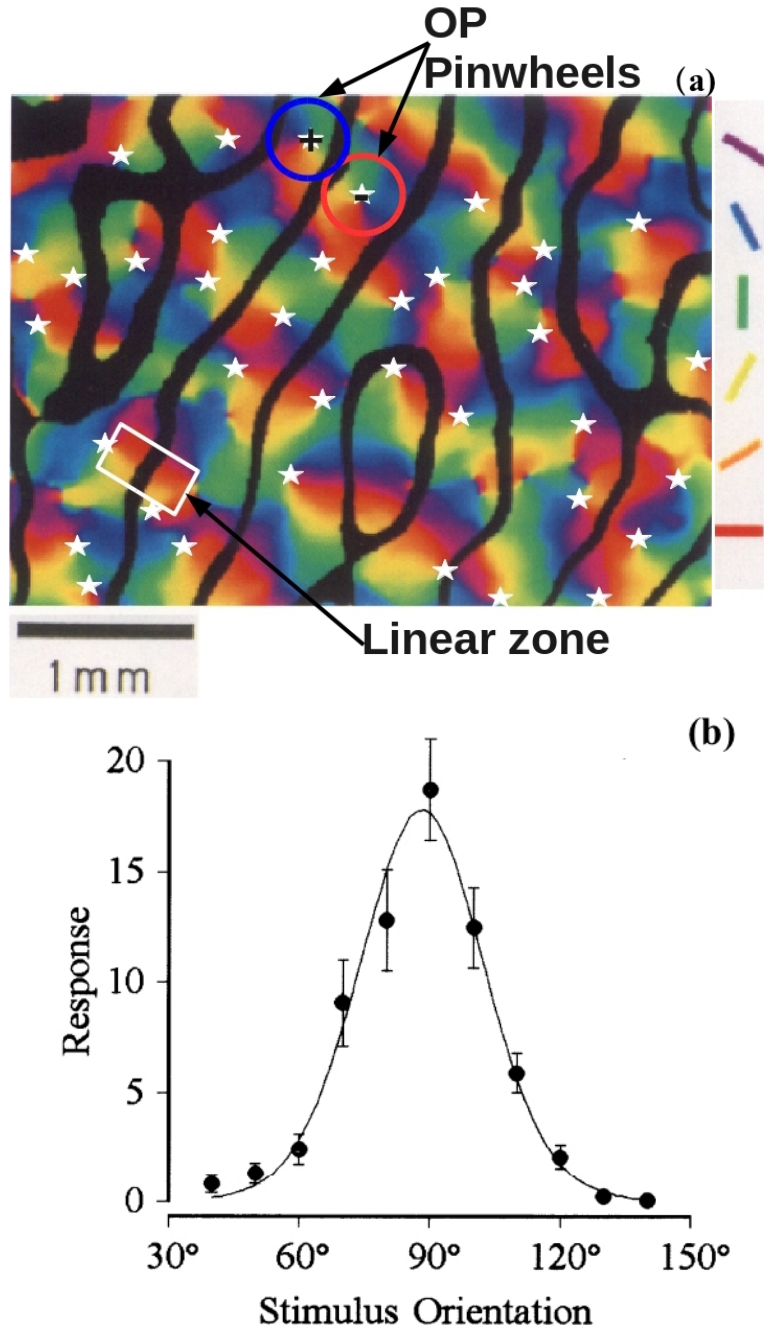


Figure 1: (a) Combined OP-OD map of macaque monkey, adapted from Blasdel (1992). The borders of OD stripes are shown in solid black, and singularities (pinwheel centers) are labeled by white stars. Oriented color bars indicate different OPs. The blue and red circles outline examples of positive and negative OP pinwheels, and the white rectangle outlines a linear zone. (b) Experimental orientation tuning curve, adapted from Swindale (1998). The preferred orientation angel is around 90°. The dots are the data points, and the solid curve is the fitted tuning curve using a von Mises function.

in nearby regions within the visual field is projected to neighboring ganglion cells in the retina. This spatial arrangement is maintained through the LGN to V1, where the visual signals are further processed by neighboring V1 neurons. The subregion in the visual field, within which certain features of the visual object tend to evoke or suppress neural firing of a given V1 neuron, is termed the receptive field (RF) of that neuron (Hubel and Wiesel, 1962a; Schiller and Tehovnik, 2015; Skottun et al., 1991; Smith et al., 2001; Tootell et al., 1982). This paper focuses on the RF of V1 simple cells, which respond best to oriented bars. The spatial RF of a V1 simple cell has separate ON (excitatory) and OFF (inhibitory) subareas, which are elongated in a specific orientation, and these subareas relate to the ON and OFF regions of LGN RFs that project to the V1 RF of a given cell. The neuron will be excited when light illuminates the ON subarea, and be depressed when light exposed to the OFF subarea (Hubel and

Wiesel, 1968; Mechler and Ringach, 2002). It was first proposed by Hubel and Wiesel (1962a) that the RF of a V1 simple cell can be predicted by a feed-forward model. Specifically, they suggested that RF of a V1 simple cell is formed by combining the circular RFs of several LGN cells to produce an elongated RF with central ON region flanked by OFF regions. Figure 2 shows a schematic of this feed-forward model, which produces a RF with a three-lobed pattern, as shown in the bottom left corner. In addition, several studies have suggested that the lateral intracortical excitatory and inhibitory connectivities from surrounding neurons also play important roles in a cell’s orientation tuning and RF formation (Ferster and Miller, 2000; Finn et al., 2007; Gardner et al., 1999; Mariño et al., 2005; Moore IV and Freeman, 2012). Moreover, some studies have discussed the relationship between the size of the RF and the width of the orientation tuning curve (Hubel and Wiesel, 1962a; Lampl et al., 2001). These authors predicted that the width of orientation tuning curve should be inversely associated with the elongation of the RF.

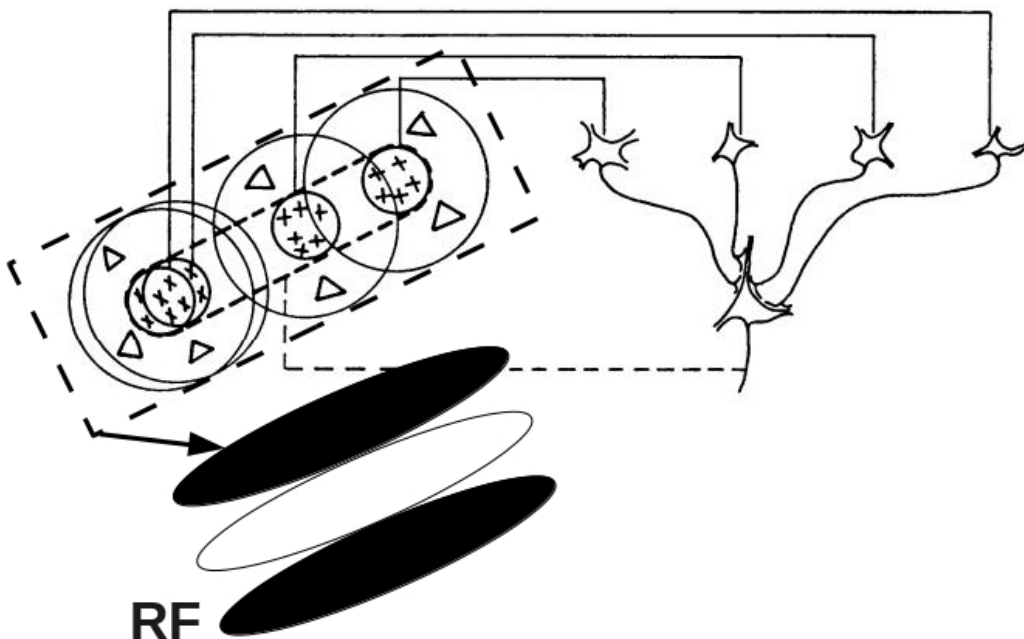


Figure 2: Schematic of the elongated RF of a V1 simple cell, showing the convergence of several LGN RFs into the V1 RF. The four cells in the right half of the figure represents LGN cells with circular ON center, OFF surround RFs. The outputs of these LGN cells project to form the elongated V1 RF shown at the bottom left. Adapted from Hubel and Wiesel (1962a).

Numerous experiments have used optical imaging or functional magnetic resonance imaging (fMRI) to reveal the spatial structure of the OP-OD map in mammals including humans (Bartfeld and Grinvald, 1992; Blasdel, 1992; Bonhoeffer and Grinvald, 1991, 1993; Bosking et al., 1997; Obermayer and Blasdel, 1993; Yacoub et al., 2008). Additionally, a number of neural network models have been proposed for the development of OP-OD maps and simulated numerically (Bednar, 2009; Erwin et al., 1995; Obermayer et al., 1992b; Swindale, 1992; Miikkulainen et al., 2005; Stevens et al., 2013). The resulting OP-OD maps obtained from experiments or simulation are only semiregular, as illustrated in Fig. 1(a). Hence, it usually requires many data points to describe the structure of such maps, which impedes understanding and requires extensive computation to integrate OP-OD maps into models of neural activity in V1. Such

models would benefit from a compact analytic representation of the OP-OD map; e.g., to incorporate its structure into existing spatiotemporal correlation analyses of gamma-band oscillations of neural activity using neural field theory (NFT), or to understand propagation via patchy neural connections in V1 (Robinson, 2005, 2006, 2007; Liu et al., 2020). These issues motivate us to derive a compact analytical representation of the OP-OD map for use in prediction and analysis of brain activity, and for analysis of properties of OP maps obtained from *in-vivo* experiments or computer simulations.

To achieve the above aim, we first note that it has long been suggested that oriented visual features such as edges can be detected by the Laplacian operator (Marr, 1982; Marr and Hildreth, 1980; Marr and Ullman, 1981; Ratliff, 1965; Young, 1987). Hence, we approximate the local sensitivity of V1 neuron to the orientation of stimuli by such an operator, which we allow to be anisotropic. This operator incorporates the details of LGN receptive fields, as projected to the cortex, and any anisotropic response at V1, as implemented through local excitatory and inhibitory wiring between neurons. Secondly, we introduce an RF operator to approximate the anisotropy of the visual region that projects activity to a given V1 simple cell. The combined Laplacian and RF operators yield an overall OP operator at each point, whose parameters can be fitted to yield observed OP tuning widths. Thirdly, we allow the properties of the OP operator to vary across V1 approximately periodically, as described by dominant Fourier coefficients.

The paper is structured as follows: Section 2 approximates the hypercolumn with its structure being compatible with the general features of OP-OD map. Meanwhile, it also is compatible with NFT. In Sec. 3, we describe the local sensitivity to stimulus orientation by applying an anisotropic Laplacian operator to the stimulus. A RF operator is then introduced to project activity from neighboring neurons to a given point. The resulting combined OP operator maximizes the response of V1 neurons to their preferred stimulus orientation and its parameters are adjusted to match experimental tuning curves. In Sec. 4, we Fourier decompose the OP variation on the period of an idealized hypercolumn and investigate the properties of the resulting Fourier coefficients. The results are then applied to compactly represent and analyze OP maps generated from widely used simulation models are then investigated in Sec. 5. Finally, the results are discussed and summarized in Sec. 6.

2 Hypercolumns and OD-OP maps

In this section, an approximate OP-OD map within a hypercolumn is proposed, which reproduces the main aspects of observed maps. It is Fourier decomposed in later sections to generate a sparse set of Fourier coefficients that can be used in NFT to study activity across many hypercolumns.

2.1 Hypercolumn arrangement

All feature preferences within a small visual field are mapped to a hypercolumn in V1 (Hubel and Wiesel, 1962b, 1974a; Miikkulainen et al., 2005). Based on the pinwheel model introduced by De Valois and De Valois (1990), we approximate the hypercolumn as a square domain, which consists of left and right OD stripes of equal width; each OD stripe contains a pair of positive and negative pinwheels for continuous (except at pinwheel centers) feature preference coverage within a hypercolumn. The hypercolumn is consistent with general observations of visual cortical map formation from experimental studies (Adams et al., 2007; Bartfeld and Grinvald, 1992; Bonhoeffer and Grinvald, 1991; Erwin et al., 1995; Müller et al., 2000; Obermayer et al., 1992a; Obermayer and Blasdel, 1993), including that: (i) left-eye and right-eye OD columns are arranged as alternating stripes in V1 of average width $a \approx 1$ mm; (ii) OP angles are arranged as pinwheels; (iii) each pinwheel center coincides with the center of its OD band; (iv) OP is continuous at OD boundaries; and (iv) neighboring pinwheels have opposite signs. A $+$ sign denotes a counterclockwise increase of OP around the pinwheel center, whereas a $-$ sign denotes a clockwise increase. According to the rules described above, two distinct arrangements of the hypercolumn are possible, as illustrated in Fig. 3, where each hypercolumn is $2a$ wide. Pinwheel arrangement I in Fig. 3(a) is used for further study in later sections, without loss of generality. However, other arrangements produce analogous results due to the fact that the hypercolumn are assumed to be continuous at boundary and periodic across V1, and other hypercolumn arrangements can be obtained by either rotating the pinwheels clockwise/counterclockwise or swapping the left/right column or top/bottom row horizontally or vertically of Fig. 3(a). Note also that one is free to consider a hypercolumn whose lower left corner is at the center of the current hypercolumn in Fig. 3(a). Such a hypercolumn has exactly the same structure as in Fig. 3(b), except for interchange of the left- and right-eye columns.

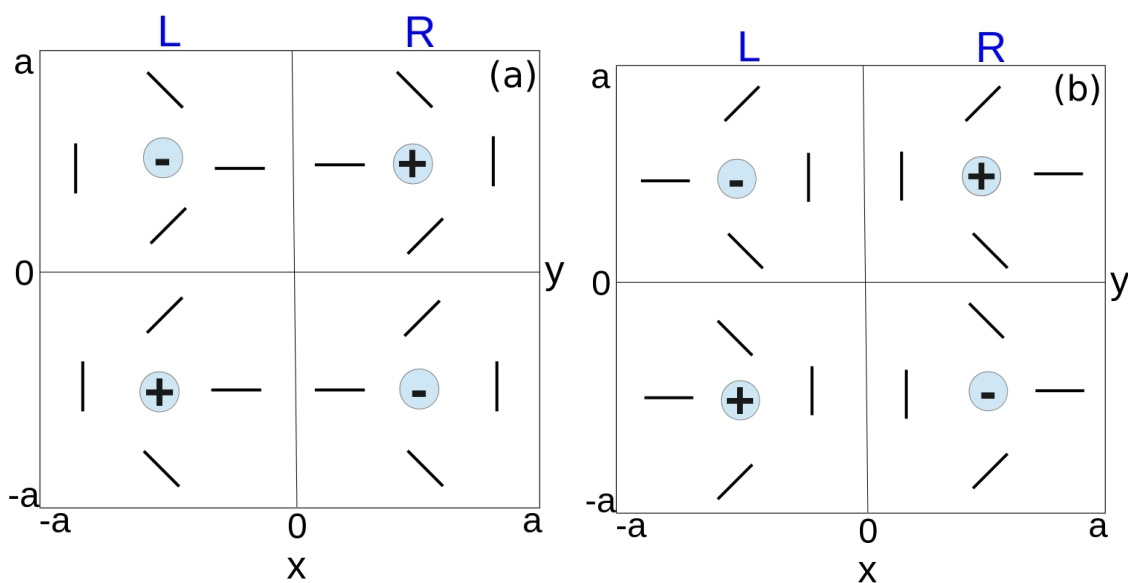


Figure 3: Schematics of possible hypercolumn arrangements. The two vertical columns of each hypercolumn represent the left and right OD bands. The orientated bars represent the OP within a pinwheel, and the $+/ -$ signs indicate the polarity of the pinwheels. (a) Pinwheel arrangement I. (b) Pinwheel arrangement II.

2.2 Single OP pinwheel structure

Our model determines the OP as a function of cortical location within each hypercolumn. The spatial coordinates of the hypercolumn are set by placing the origin of the coordinates at the center of the hypercolumn, whose boundaries are at $x = \pm a$ and $y = \pm a$, as shown in Fig. 3. The four pinwheels in a single hypercolumn are modeled by first generating the right-top pinwheel, and other pinwheels are produced by mirroring the right-top pinwheel across the x -axis, the y -axis, and then both. When generating the right-top pinwheel, the x and y coordinates range from 0 to a and the OP angle $\varphi(x, y)$ at each cortical position (x, y) is approximated by the inverse tangent function defined in Eq. (1).

$$\varphi(x, y) = \frac{1}{2} \begin{cases} \arctan\left(\frac{y-y_0}{x-x_0}\right), & x > x_0, y > y_0 \\ \frac{\pi}{2}, & x = x_0, y > y_0 \\ \arctan\left(\frac{y-y_0}{x-x_0}\right) + \pi, & x < x_0, y > y_0 \\ \frac{3\pi}{2}, & x = x_0, y < y_0 \\ \arctan\left(\frac{y-y_0}{x-x_0}\right) + 2\pi, & x > x_0, y < y_0 \end{cases} \quad (1)$$

where $(x_0, y_0) = (a/2, a/2)$ is the center of the right-top pinwheel. The $1/2$ coefficient in front of the inverse tangent functions is to make the range of $\varphi(x, y)$ to be 0° to 180° .

The negative and positive pinwheels on the top half of hypercolumn are illustrated in Figs 4(a) and (b). Figure 4(c) shows a hypercolumn containing four pinwheels. As mentioned previously, the OP and OD features are approximated as continuous and periodic for the moment, so V1 can be approximated as lattice of hypercolumns. Thus, we can construct an array of our approximated hypercolumns to represent a piece of V1, which is shown in Fig. 4(d). In such an array, the OP structure resembles maps reconstructed from *in-vivo* experiments (e.g., Fig. 1(a)), although the OD stripes are approximated as straight here (Blasdel, 1992; Bonhoeffer and Grinvald, 1991, 1993; Obermayer and Blasdel, 1993).

3 OP Operator

In this section, we derive analytic representations for the OP of V1 neurons. Firstly, we adopt an anisotropic Laplacian operator to describe the local response of the system to an edge, which can include both the near-isotropic response of the LGN plus any anisotropy introduced by local wiring in V1. We also introduce the RF operator that describes the projection of activity from nearby neurons in an anisotropic surrounding region. The combination of these two operators gives an over OP operator, whose parameters we fit to match experimental tuning curves.

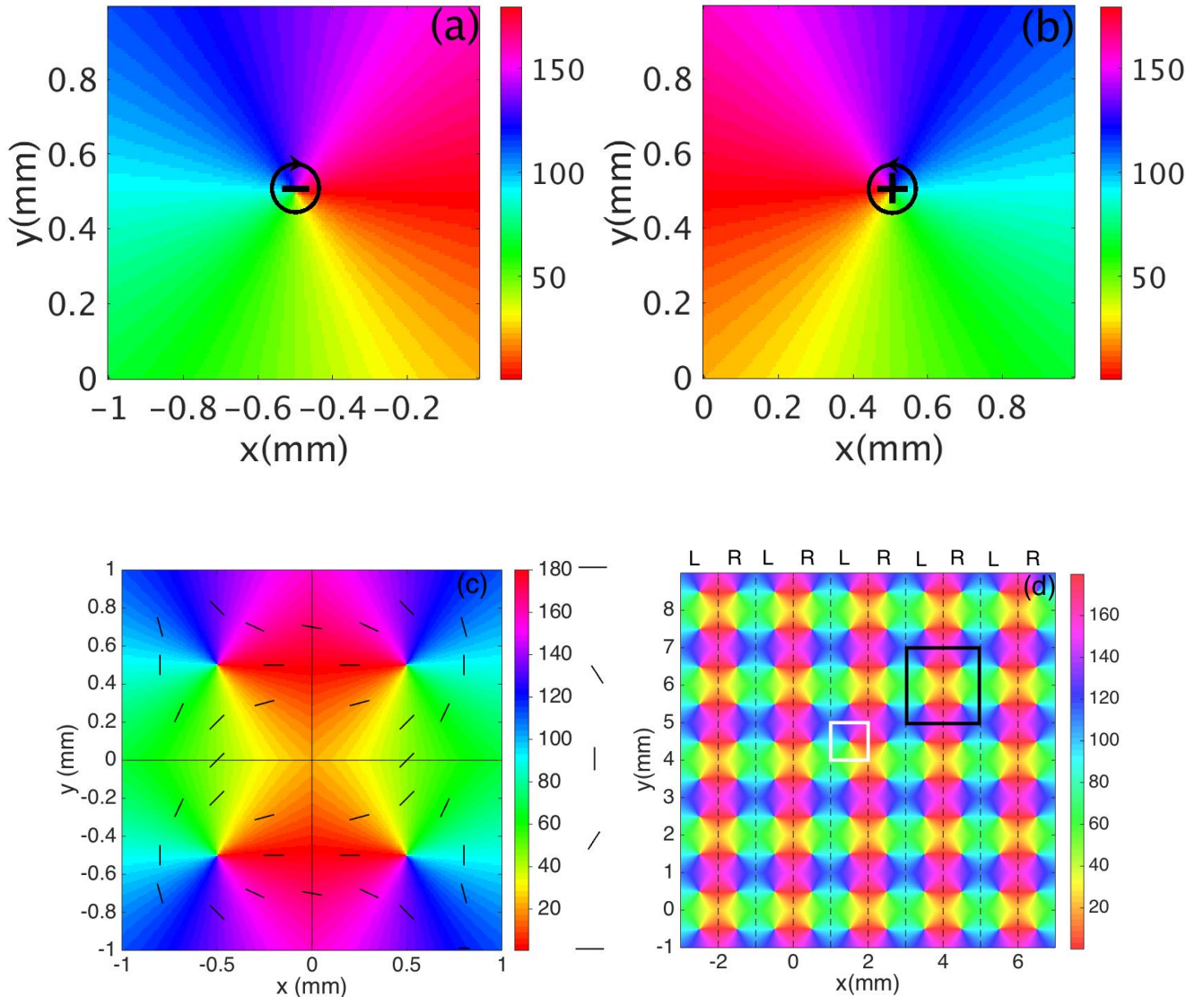


Figure 4: Schematics of visual feature preference maps in V1 with color bars indicating OP in degrees. (a) Negative pinwheel. (b) Positive pinwheel. Both pinwheels are 180° periodic. (c) Hypercolumn. The vertical line divides the hypercolumn into left and right OD columns of equal width, while the horizontal and vertical lines split the hypercolumn into four squares, each containing one OP pinwheel. The short bars highlight the OP at various locations. The 0° and 180° orientations both appear as horizontal bars. (d) Periodic spatial structure of OP and OD columns across a small piece of V1 comprising 25 hypercolumns. Dashed lines bound left (L) and right (R) OD columns. One pinwheel is outlined in white and one hypercolumn is outlined in black.

3.1 Anisotropic Laplacian (AL) Operator

In computer vision, edges with different orientation can be detected by linearly combining the second-order partial derivatives of the input (Marr and Hildreth, 1980; Marr, 1982; Torre and Poggio, 1986). Similarly, we can model the local sensitivity of V1 neurons to stimulus orientation, by calculating the weighted sum of the second-order partial derivatives of activity projected from the oriented bar stimuli, using rotated axes for simplicity. Figure 5 shows an original $x - y$ coordinate system, and $x' - y'$ axes obtained by rotating the original axes by an OP angle φ that is the angle of an oriented bar.

A short bar in an image gives rise to localized, anisotropic intensity changes (Torre and Poggio, 1986). In the rotated coordinates, this 2-dimensional intensity change can be detected by the weighted second order partial derivatives in the x' and y' directions. Hence, we define an anisotropic Laplacian

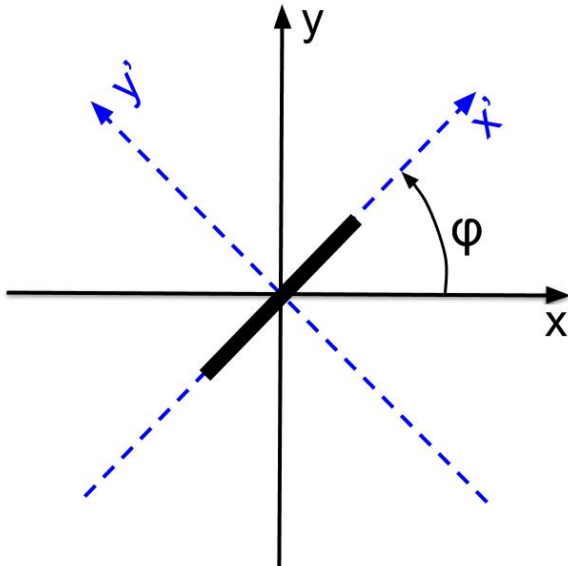


Figure 5: Coordinates used to analyze the anisotropic Laplacian operator. Original axes x and y are shown in solid, while the rotated axes x' and y' are dashed. The input stimulus is a bar oriented at angle φ .

operator \mathcal{P} as a weighted linear combination of the second order partial derivatives:

$$\mathcal{P} = a^2 \frac{\partial^2}{\partial x'^2} + b^2 \frac{\partial^2}{\partial y'^2}, \quad (2)$$

where the rotated coordinates satisfy

$$x' = x \cos \varphi + y \sin \varphi, \quad (3)$$

$$y' = -x \sin \varphi + y \cos \varphi, \quad (4)$$

where the OP φ ranges from 0 to π , and a^2 and b^2 are constants.

Taking the Fourier transform of both sides of Eq. (2) yields

$$\mathcal{P}(\mathbf{k}) = -a^2 k_{x'}^2 - b^2 k_{y'}^2, \quad (5)$$

where

$$k_{x'}^2 = (k_x \cos \varphi + k_y \sin \varphi)^2, \quad (6)$$

$$k_{y'}^2 = (-k_x \sin \varphi + k_y \cos \varphi)^2. \quad (7)$$

Substituting Eqs (6) and (7) into Eq. (5) and then performing inverse Fourier transform yields

$$\mathcal{P} = (a^2 \cos^2 \varphi + b^2 \sin^2 \varphi) \frac{\partial^2}{\partial x^2} + (a^2 - b^2) \sin(2\varphi) \frac{\partial^2}{\partial x \partial y} + (a^2 \sin^2 \varphi + b^2 \cos^2 \varphi) \frac{\partial^2}{\partial y^2}. \quad (8)$$

Since the stimulus S is oriented along the x' axis, we would need more weight on $\partial^2/\partial y'^2$ than on $\partial^2/\partial x'^2$

to have a maximal response to the desired orientation; this implies that $b^2 \geq a^2$.

3.2 Receptive field (RF) operator

Previous studies (Ferster and Miller, 2000; Finn et al., 2007; Hubel and Wiesel, 1977; Mariño et al., 2005; Toth et al., 1997; Schummers et al., 2002; Troyer et al., 1998) have suggested that the orientation tuning of V1 neuron is altered by the excitatory (inhibitory) inputs from locally connected neighboring neurons (either from the same orientation column or from neighboring columns). Thus, we now introduce an RF operator to model the anisotropic RF that projects to V1 cells. This consists of a weight function $G(\mathbf{R} - \mathbf{r})$, which describes the strength of the neural projection from \mathbf{R} to a cell at \mathbf{r} . Figure 6 shows the schematic of the RF operator on a piece of cortex. It shows the location \mathbf{r} of the cells whose OP is being approximated and locations \mathbf{R} whose activity projects to \mathbf{r} .

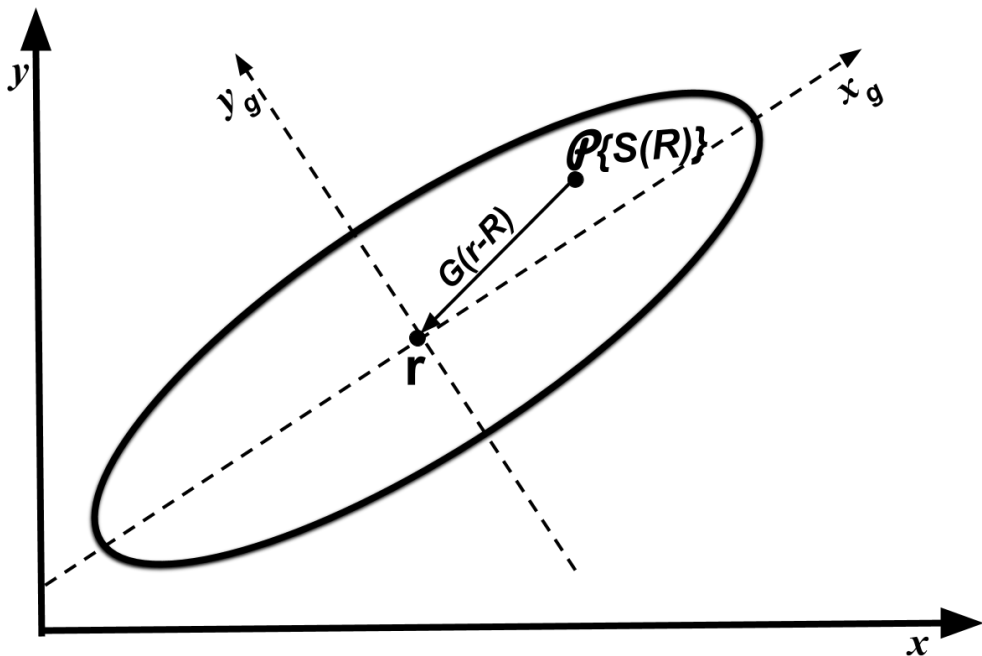


Figure 6: Schematic of operators leading to the OP response at cells at \mathbf{r} on the cortex. An oriented bar is mapped to locations \mathbf{R} in the receptive field, which projects to \mathbf{r} via the anisotropic weight function $G(\mathbf{r} - \mathbf{R})$ indicated by the solid elliptic contour. The local anisotropic Laplacian operator \mathcal{P} then acts at \mathbf{r} . The arrow shows how the neural response are project to measurement point \mathbf{r} via the weight function. The x_g and y_g are the major and minor axis of the weight function, respectively.

We approximate $G(\mathbf{r} - \mathbf{R})$ as an anisotropic Gaussian function whose long axis is oriented at the local OP φ at \mathbf{R} (Jones and Palmer, 1987). If $\mathbf{R} = (x_R, y_R)$ and $\mathbf{r} = (x, y)$, we have

$$G(\mathbf{r} - \mathbf{R}) = \frac{1}{2\pi\sigma_x\sigma_y} \exp \left[-\frac{1}{2} \left(\frac{x_g^2}{\sigma_x^2} + \frac{y_g^2}{\sigma_y^2} \right) \right], \quad (9)$$

where

$$x_g = (x - x_R) \cos \varphi + (y - y_R) \sin \varphi, \quad (10)$$

$$y_g = -(x - x_R) \sin \varphi + (y - y_R) \cos \varphi. \quad (11)$$

The appropriate width of $G(\mathbf{r} - \mathbf{R})$ along the x_g axis is determined by two factors: (i) the approximate

RF size near the fovea measured from experiments. Previous studies (Dow et al., 1981; Hubel and Wiesel, 1974b; Keliris et al., 2019) yielded an RF size of $\approx 0.082^\circ$ at the eccentricity of 1° in macaque Monkey. We then transform the RF size in visual degree to the corresponding cortical size in mm by adopting the magnification factor (mm/deg) from Horton and Hoyt (1991), where the magnification factor M in Monkey is approximated as

$$M = \frac{12}{E + 0.75}, \quad (12)$$

where E is the eccentricity in degrees. The corresponding cortical RF size is then ~ 0.56 mm; (ii) the width of the weight function should ensure an approximate 30° fall off from the measuring neuron's maximum response when it is activated by its optimal orientation (De Valois et al., 1982; Moore IV and Freeman, 2012; Gur et al., 2005; Ringach et al., 2002; Swindale, 1998). In order to satisfy both factors, we choose $\sigma_x = 0.16$ mm.

3.3 Combined OP operator

Here we combine the anisotropic Laplacian and RF operators from above to obtain an overall OP operator and adjust its parameters to match experimental OP tuning curves.

The input at location \mathbf{R} is approximated by applying the AL operator to the stimulus S (i.e., $\mathcal{P}\{S(\mathbf{R})\}$ in Fig. 6), so that the local orientation sensitivity is picked out, while the weight function $G(\mathbf{R} - \mathbf{r})$ determines how much response from locations \mathbf{R} are projected to \mathbf{r} . Hence, the response at \mathbf{r} can be approximated by convolving the weight function with the OP operator on the stimulus at different location \mathbf{R} . It can be written as

$$I(\mathbf{r}) = \int G(\mathbf{r} - \mathbf{R}) \mathcal{P}\{S(\mathbf{R})\} d\mathbf{R}. \quad (13)$$

In the Fourier domain, the convolution theorem yields

$$I(\mathbf{k}) = G(\mathbf{k}) \mathcal{P}(\mathbf{k}) S(\mathbf{k}). \quad (14)$$

where the algebraic function $\mathcal{P}(\mathbf{k})$ is defined in Eq. (5). We can thus reverse the order of $\mathcal{P}(\mathbf{k})$ and $G(\mathbf{k})$ on the right hand side of Eq. (14) and inverse Fourier transform to obtain

$$I(\mathbf{r}) = \int \mathcal{P}\{G(\mathbf{r} - \mathbf{R})\} S(\mathbf{R}) d\mathbf{R}. \quad (15)$$

Hence, the response at \mathbf{r} becomes the convolution of a new combined OP operator $\mathcal{P}\{G(\mathbf{r} - \mathbf{R})\}$ with the stimulus itself. This result agrees with previous studies (Graham, 1989; Movshon et al., 1978), which indicated that V1 simple cell can be modeled as a linear filter and its responses are computed as the weighted integral of the Laplacian-transformed stimulus, with the weights given by the RF pattern.

Figure 7(a) shows a contour plot of the RF operator $\mathcal{P}\{G(\mathbf{r}-\mathbf{R})\}$ with a preferred orientation angle of $\varphi = 22.5^\circ$. The operator has an elongated three-lobe pattern with its major axis along the direction φ , with an ON center lobe and two OFF side lobes. Figure 7(b) shows a measured RF of V1 simple cells of macaque monkey (Ringach, 2002), showing that our OP operator closely resembles the experimental one in spatial structure.

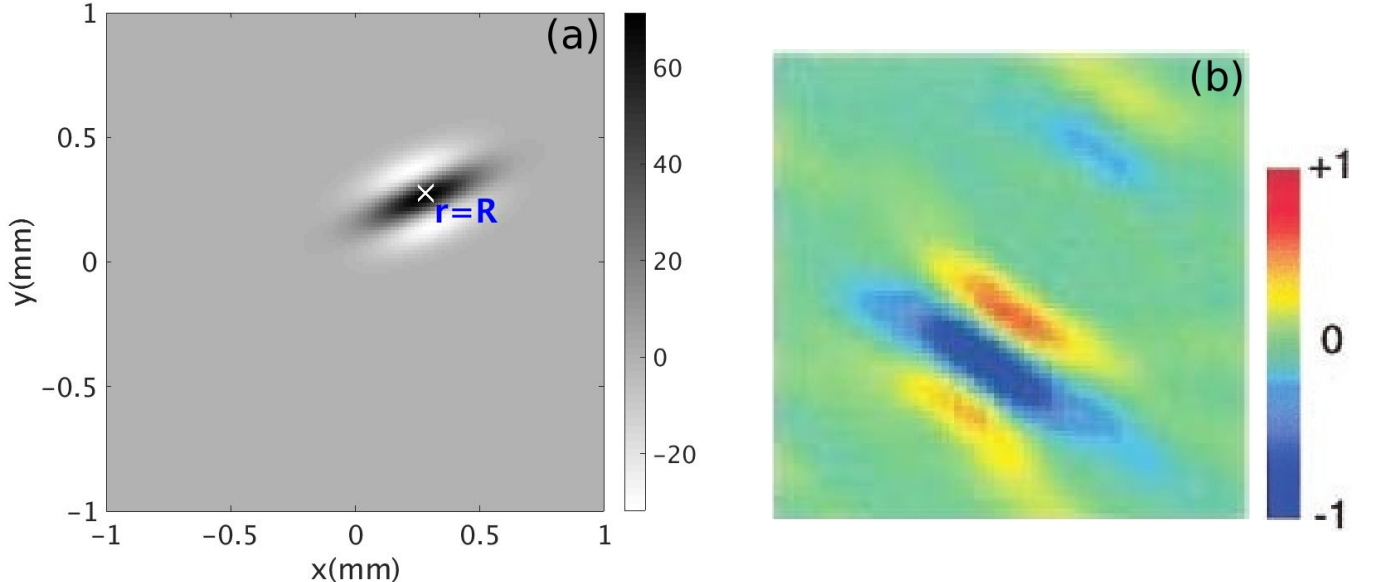


Figure 7: (a) Receptive field operator $\mathcal{P}\{G(\mathbf{R}-\mathbf{r})\}$ with OP=22.5°. The color bar indicates the amplitude of the operator. (b) RF of macaque monkey V1 simple cell from experiment (Ringach, 2002). The color bar indicates normalized impulse response strength of the neurons.

3.4 Angular selectivity of the OP operator

The full width at half maximum (FWHM) of the bell-shaped OP angle tuning curve plotted from the neuron response by convolving the RF operator and the stimulus can be used to parameterize the OP selectivity of the RF operator. The parameters are tunable by adjusting the ratio σ_x^2/σ_y^2 of the weight function $G(\mathbf{r}-\mathbf{R})$ defined in Eq. (9), and the ratio b^2/a^2 of the anisotropic Laplacian operator \mathcal{P} defined in Eq. (8). Hence, we can find the optimal parameter values of the combined OP operator by adjusting its parameters so its tuning curve matches experiment.

We first vary the values of a^2 and b^2 while keeping their sum constant by writing

$$a^2 = \sin^2 \psi, \quad (16)$$

$$b^2 = \cos^2 \psi, \quad (17)$$

where ψ ranges from 0 to $\pi/4$ to ensure $b^2 \geq a^2$. We also vary the ratio σ_x/σ_y from 1.5 to 6.5 to elongate the weight function along the x_g axis defined in Eq. (10). Figure 8 shows the resulting contour map of the FWHM vs. b^2/a^2 and σ_x/σ_y . The FWHM varies rapidly with σ_x/σ_y , with sharper tuning as σ_x/σ_y increases. In contrast, the FWHM only sharpens slightly when b^2/a^2 increases.

In order to illustrate the insensitivity of the FWHM to b/a more clearly, Fig. 9(a) shows the nor-

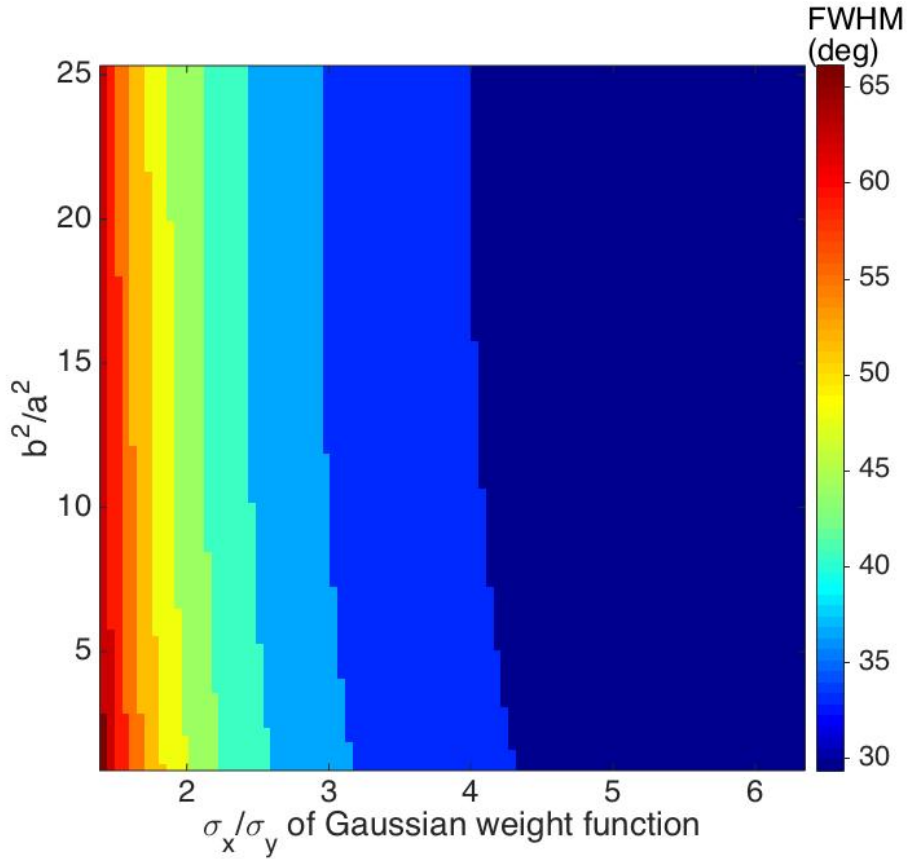


Figure 8: Contour map of the FWHM of the OP tuning curve vs b^2/a^2 , and σ_x/σ_y . The preferred orientation angle at measurement point is 135° . The value of σ_x/σ_y is given by x axis, and the ratio of b^2 and a^2 is given by y axis. The color bar represents the FWHM width in degrees.

malized tuning curves for fixed $\sigma_x/\sigma_y = 2.5$, varying b^2/a^2 from 1 to 100. The FWHM decreases by only $\sim 2^\circ$ when b^2/a^2 changes from 1 to 5, and it does not decrease significantly further for larger b^2/a^2 . The reason for this is that the RF operator envelope defined by $G(\mathbf{r} - \mathbf{R})$ limits the effective lengths of its three lobes to the Gaussian envelope's characteristic width, so they do not change much when b^2/a^2 increases. This agrees with the predictions of previous studies, which argued that the OP tuning width of a V1 simple cell varies inversely with the size of its RF (Hubel and Wiesel, 1962a; Lampl et al., 2001). It is also consistent with the Gaussian derivative model proposed by Young et al. (2001) for modeling the spatiotemporal RF of V1 cells. Our results also match Hubel and Wiesel's feed-forward model, in which the overall V1 RF results from the net effect of aggregating isotropic LGN RFs via anisotropic connections in V1 (Hubel and Wiesel, 1962a).

The above analysis implies that we can simplify the OP operator by setting $b^2 = a^2$ because their ratio does not affect the OP tuning width significantly. Then the OP operator $\mathcal{P}\{G(\mathbf{r} - \mathbf{R})\}$ becomes the Laplacian of the weight function $\mathcal{L}\{G(\mathbf{r} - \mathbf{R})\}$ and the tuning width is controlled by the elongation of the weight function $G(\mathbf{r} - \mathbf{R})$.

Previous studies suggested that the FWHM of orientation tuning curve of most V1 neurons is 35° to 40° (De Valois et al., 1982; Gur et al., 2005; Ringach et al., 2002; Swindale, 1996). This corresponds to σ_x/σ_y ranging roughly from 2.3 to 3.2 in Fig. 8. Thus, to be consistent with experimental results, we choose $\sigma_x/\sigma_y = 2.6$ and $b^2 = a^2$, which gives a FWHM of 37° and the tuning curves shown in Fig. 9(b).

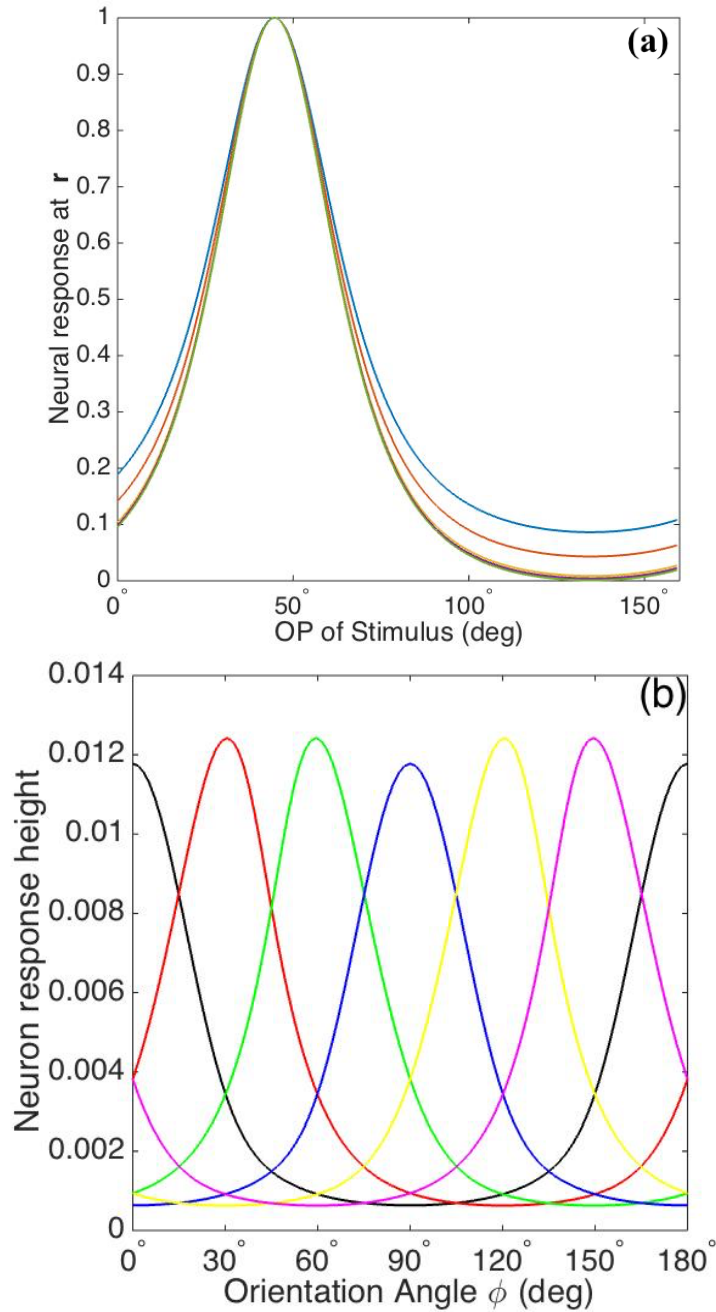


Figure 9: (a) Normalized tuning curves with b^2/a^2 set to 1 (blue), 2 (red), 10 (yellow), 20 (purple), and 100 (green); and fixing $\sigma_x/\sigma_y = 2.5$. The preferred orientation angle is set to 45° . (b) OP tuning curves with orientation angles 0° (black), 30° (red), 60° (green), 90° (blue), 120° (yellow), 150° (purple), and 180° (black), with $\sigma_x/\sigma_y = 2.6$ and $b^2/a^2 = 1$.

3.5 Tuning curves vs. Distance to Pinwheel Center

The tuning curve of a cell (e.g., located at \mathbf{r}_0) describes its responses to different OPs. We compute the overall response of the cell for a particular OP [i.e., $I_{OP}(\mathbf{r}_0)$] by taking a weighted average of the neural responses within a small circular region surrounding the cell and tightly coupled to it; this is achieved by integrating the responses of all the cells with a Gaussian weight function over the region:

$$I_{OP}(\mathbf{r}_0) = \int I(\mathbf{r})W(\mathbf{r} - \mathbf{r}_0)d\mathbf{r}, \quad (18)$$

where

$$W(\mathbf{r} - \mathbf{r}_0) = \frac{1}{2\pi\sigma_r^2} \exp \left[-\frac{(\mathbf{r} - \mathbf{r}_0)^2}{2\sigma_r^2} \right]. \quad (19)$$

The width of the weight function is set to $40\ \mu\text{m}$, to approximate the characteristic width of an OP microcolumn and the experimental range of pinwheel-center effects on OP selectivity (Maldonado et al., 1997; Nauhaus et al., 2008; Obermayer and Blasdel, 1993; Ohki et al., 2006).

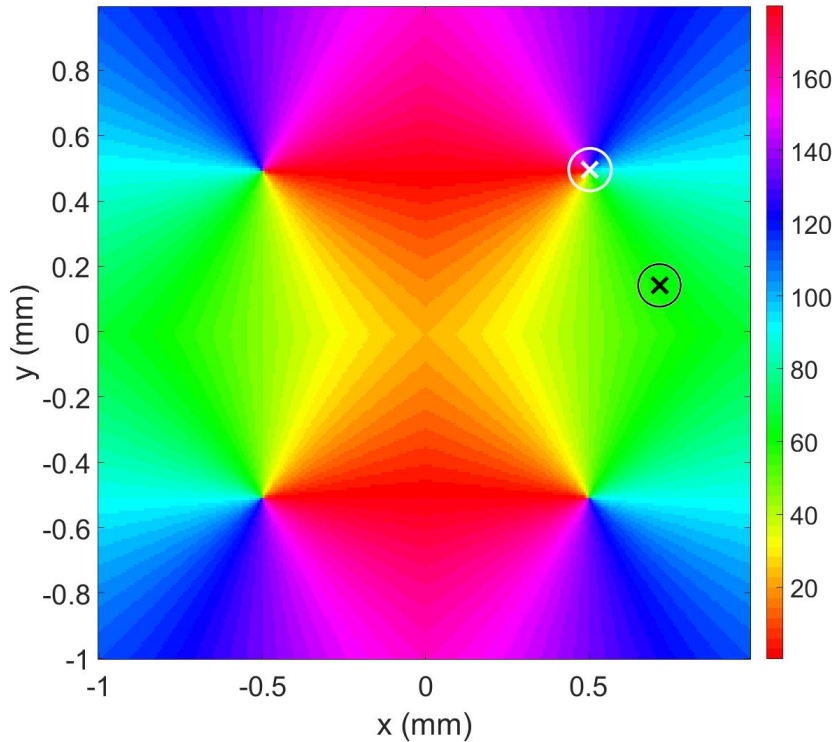


Figure 10: Locations of cells in a hypercolumn for computing the tuning curves. Cells near a pinwheel center and in an iso-orientation domain are marked with crosses, and the circle around each indicates the characteristic width of the integration region. The color bar shows the orientation angle in degrees.

We consider two cases of tuning curves for cells with different locations in the hypercolumn, one near a pinwheel center and another one in an iso-orientation domain. These locations are marked with crosses in Fig. 10, and the circle around each cross indicates the characteristic width of the weight function in Eq. (18). Figure 11(a) shows the resulting tuning curve of the overall responses of the cell located in an iso-orientation domain (i.e., the location marked with black cross in Fig. 10) with preferred orientation $\approx 60^\circ$. It is sharply peaked at the preferred angle with FWHM $\approx 41^\circ$. In Fig. 11(b), we plot the tuning curves for an array of cells that are around the measurement site within the circular region. Since all the cells are located in the iso-orientation domain, they have very similar orientation preferences and tuning curves. The overall response of the cell near the pinwheel center is plotted in Fig. 11(c), it is much broader than the tuning curve shown in Fig. 11(a) due to the fact that we average the responses from neurons with a wide range of OPs, as shown in Fig. 11(d). Our predictions agree with the experimental results (Maldonado et al., 1997; Ohki et al., 2006), who found that individual neurons near the pinwheel center are just as orientation selective as the ones in the iso-orientation domain, and the overall broadly tuned response is the averaged response of nearby cells with a wide range of OPs.

We have also investigated how the tuning width and response strength vary with distance from the pinwheel center, and compare them with experiment in Fig. 12. We calculate half width at half maximum (HWHM) here, in order to be consistent with the experimental plots. As expected, our predicted HWHM

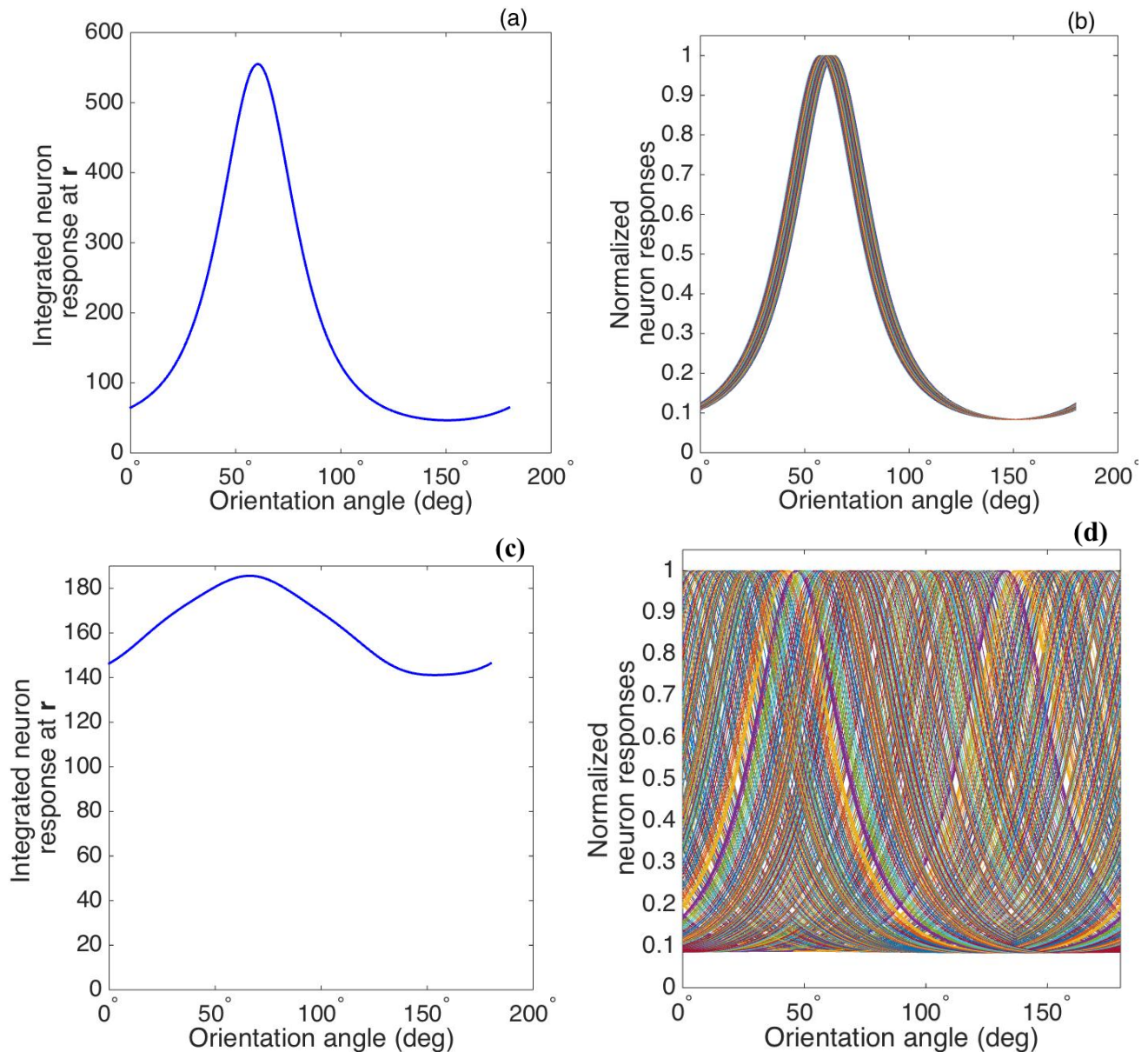


Figure 11: (a) Tuning curve of averaged responses at measurement site located in iso-orientation domain (i.e. marked as black cross in Fig. 10). (b) Tuning curves of all the cells surrounding the measurement site within the circular region in iso-orientation domain. (c) Tuning curve of averaged responses at measurement site located near pinwheel center (i.e. marked as white cross in Fig. 10). (d) Tuning curves of all the cells surrounding the measurement site within the circular region near pinwheel center.

decreases when moving away from the pinwheel center to an iso-orientation domain, while the response strength increases with the distance (Fig. 12(b)). Both results match the experimental findings shown in Fig. 12(a), except the experimental HWHM in iso-orientation domain is wider than ours; However, our plots do not reproduce the overshoot and dip in the responses strength and HWHM curves, respectively, shown in Fig. 12(a). In order to achieve a better fit to the experimental data, we thus try the Mexican hat function,

$$W_{mex}(\mathbf{r} - \mathbf{r}_0) = \left[1 - \frac{(\mathbf{r} - \mathbf{r}_0)^2}{2\sigma_r^2} \right] \exp \left[-\frac{(\mathbf{r} - \mathbf{r}_0)^2}{2\sigma_r^2} \right]. \quad (20)$$

as the weight function to average the responses, and the resulting plots are shown in Fig. 12(c). Overshoot and dip features are visible in this case, implying a better match. Thus, it is potentially possible to deduce the shape of the weight function from experimental results such as these, but detailed exploration is beyond the scope of the present paper.

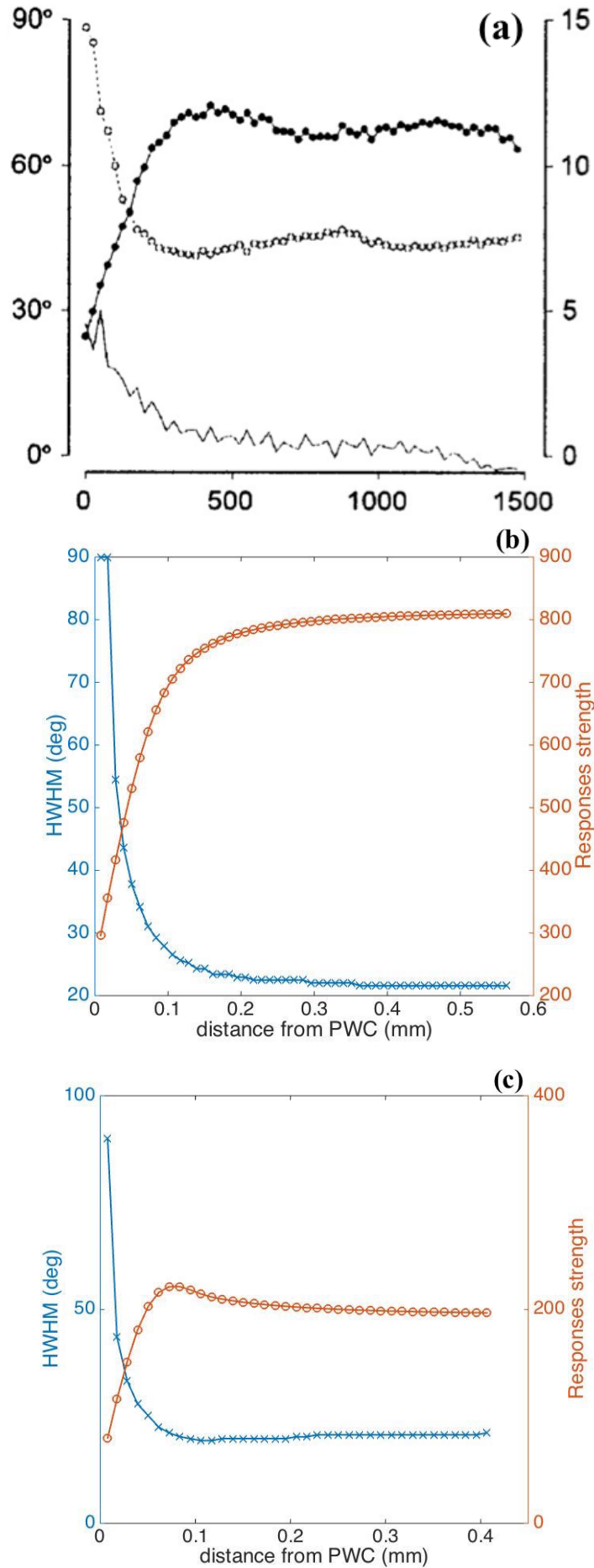


Figure 12: (a) Experimental HWHM and response strength vs. distance in μm from pinwheel center from Swindale et al. (2003), averaged over 13 pinwheels. The filled circles shows the response strength in arbitrary units, while the open circles show the HWHM in degrees and the bottom-most curve shows the baseline activity. (b) Predicted HWHM vs. distance (blue) and Responses strength vs. distance (orange) from pinwheel center, by using Gaussian function as weight function for averaging the responses. (c) Predicted HWHM vs. distance (blue) and Responses strength vs. distance (orange) from pinwheel center, by using Mexican hat function as weight function for averaging the responses.

4 Fourier decomposition of the OP-OD Map

We seek a representation of the OP map in the Fourier domain so that we can apply it to compactly represent experimental data and to study the spatiotemporal neural activity patterns in periodic V1 structures using NFT, which requires such Fourier coefficients as input. Thus, in this section, we decompose the OP-OD map of the hypercolumn that is defined in Sec. 2 in the Fourier domain, derive the Fourier coefficients that represents the spatial frequency components of the OP-OD map structure and discuss their properties. We also determine the least number of Fourier coefficients we need in NFT analysis while maintaining the essential features of the OP-OD map. This is achieved by reconstructing the OP-OD map with a subset of the coefficients using the inverse Fourier transform.

We decompose the OP map in the hypercolumn by first applying a spatial operator \mathcal{O} to the map, with \mathcal{O} defined as

$$\mathcal{O} = \exp [i2\varphi(x, y)]. \quad (21)$$

This operator preserves the structure and periodicity of the OP-OD map and allows us to avoid the spurious discontinuities between 0° and 180° orientations, which actually correspond to the same stimulus orientation. This is important because representation of such discontinuities would require use of high spatial frequencies, and thus many Fourier coefficients. We then perform a 2D Fourier transform on the resulting map, which yields a sparse set of Fourier coefficients.

Figure 13(a) shows the magnitude of the Fourier coefficients of a lattice of 5×5 hypercolumns [i.e., Fig. 4(d)]. We note that: (i) the coefficients have 4-fold symmetry, and the 4 lowest \mathbf{K} modes are dominant; and (ii) the lowest \mathbf{K} modes are located at $(\pm\pi/a, 0)$ and $(0, \pm\pi/a)$, where $2a$ is the width of hypercolumn.

One of our main aims in finding these Fourier coefficients of the OP-OD map is to incorporate the OP map structure into the patchy propagator theory introduced to treat periodic V1 structure in previous studies (Robinson, 2006, 2007; Liu et al., 2020). We want to use as few coefficients as possible to simplify computation, while preserving the essential OP-OD structure. In order to test how well a small subset of Fourier coefficients can approximate the OP-OD map, we reconstruct the lattice of hypercolumns from these coefficients and compare it to the original one. We first perform the inverse Fourier transform on a small subset of the coefficients. The resulting complex data represents the values that have been transformed from the OP angles after applying the operator \mathcal{O} defined in Eq. (21). We then transform the complex data back to OP angles via

$$e^{i\varphi(x,y)} = \cos[\varphi(x, y)] + i \sin[\varphi(x, y)], \quad (22)$$

whence

$$\varphi(x, y) = \tan^{-1} \left[\frac{\sin \varphi(x, y)}{\cos \varphi(x, y)} \right]. \quad (23)$$

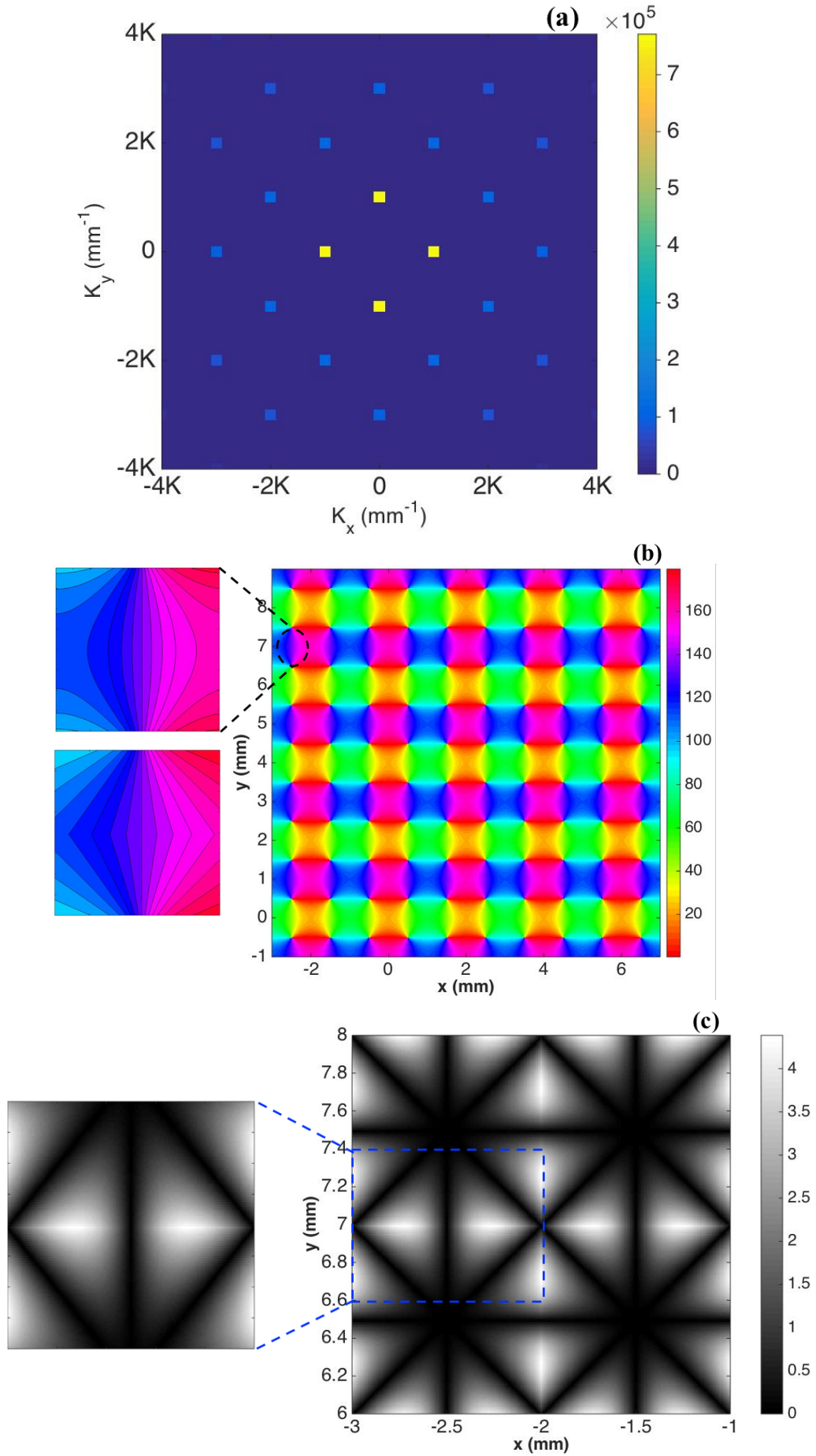


Figure 13: (a) Magnitude of Fourier coefficients of the OP-OD map after applying the operator \mathcal{O} to a lattice of 25 hypercolumns. Each square on the figure represents one spatial mode \mathbf{K} , and the color bar indicates the magnitude of it. (b) Reconstructed OP map of a lattice of 25 hypercolumns. The two squares on the top-left are the zoomed-in patches of the reconstructed (top) and the original (bottom) lattice. These are extracted from the same location that is marked by dashed-line oval. The color bar indicates the OP in degrees. (c) Absolute differences between the original hypercolumn OP in Fig. 4(c) and the reconstructed one. The square on the left shows a zoomed-in patch that are extracted from the location marked by blue dashed-line. The color bar indicates the difference in degrees.

We find that the four lowest \mathbf{K} modes (the yellow squares in Fig. 13)(a) suffice to reproduce the main features of the hypercolumn lattice, and the reconstructed OP map is shown in Fig. 13(b), which is very similar to the original one [i.e., Fig. 4(d)] except some angular contours are smoothed out due to the absence of higher- \mathbf{K} modes. This detail is shown in the top left frame of Fig. 13(b), which is to be compared with the frame below it, which is from the same part of the original lattice.

Figure 13(c) shows the absolute differences between the original hypercolumn and the reconstructed one. The square on the left is a zoomed-in patch that are marked by the dashed-line square, and it is extracted in the same location as we do for the zoomed-in patch in Fig. 13(b). The largest difference is $\approx 4.5^\circ$, and are around the edges of each pinwheel. Nevertheless, the basic structure and periodicity of the hypercolumn are all preserved in the reconstructed lattice. Thus, we can conclude that the 4 lowest \mathbf{K} modes are sufficient for incorporating the OP map structure into NFT computations.

Going beyond idealized hypercolumns, we also can model more irregular and biologically realistic OP maps by adding more spatial modes around the 4 lowest \mathbf{K} modes. We have noticed that the real OP-OD map does not have straight OD columns running vertically as we defined in Sec. 2; rather, these columns are bent and oblique. In image processing, a rotation of Fourier coefficients produces a rotation of the image in spatial domain by the same angle (Ballard and Brown, 1982). Hence, we can alter the OP-OD map by modifying the modes in Fourier domain.

Our approach for reconstructing the more realistic OP-OD map is to add the \mathbf{K} modes around the 4 lowest \mathbf{K} with its magnitude M_k defined by Gaussian envelopes in K_x , K_y , and azimuthal angle Θ , defined as,

$$M_k = \exp \left[-(\mathbf{K} - \mathbf{K}_0)^2 / 2\Delta_K^2 \right] \exp \left[-(\Theta - \Theta_0)^2 / 2\Delta_\Theta^2 \right], \quad (24)$$

where \mathbf{K}_0 and Θ_0 are the location and azimuth angle of the original lowest \mathbf{K} modes, Δ_K and Δ_Θ are the variance of the Gaussian envelope and we set these to $\frac{1}{2}K \text{ mm}^{-1}$ ($K = \pi/a$, where $2a$ is the width of the hypercolumn) and 20° , respectively, to match experimental observations. The resulting magnitude plot of \mathbf{K} modes is shown in Fig. 14(a) and reconstructed OP-OD map using this set of \mathbf{K} is shown in Fig. 14(b).

Fig. 14(b) resembles the biologically realistic OP-OD maps obtained in experiments (Blasdel, 1992; Bonhoeffer and Grinvald, 1993; Obermayer and Blasdel, 1993), and it reproduces the general observations of the OP-OD maps we mentioned in Sec. 2.1, including: (i) it has both positive and negative pinwheels, and the neighboring pinwheels have opposite signs; (ii) linear zones connect two pinwheel centers.

5 Application to OP maps from a neural network model

In order to analyze the general properties of more realistic OP maps, We perform the same Fourier analysis as on the idealized hypercolumns in previous sections for the OP-OD map generated from a

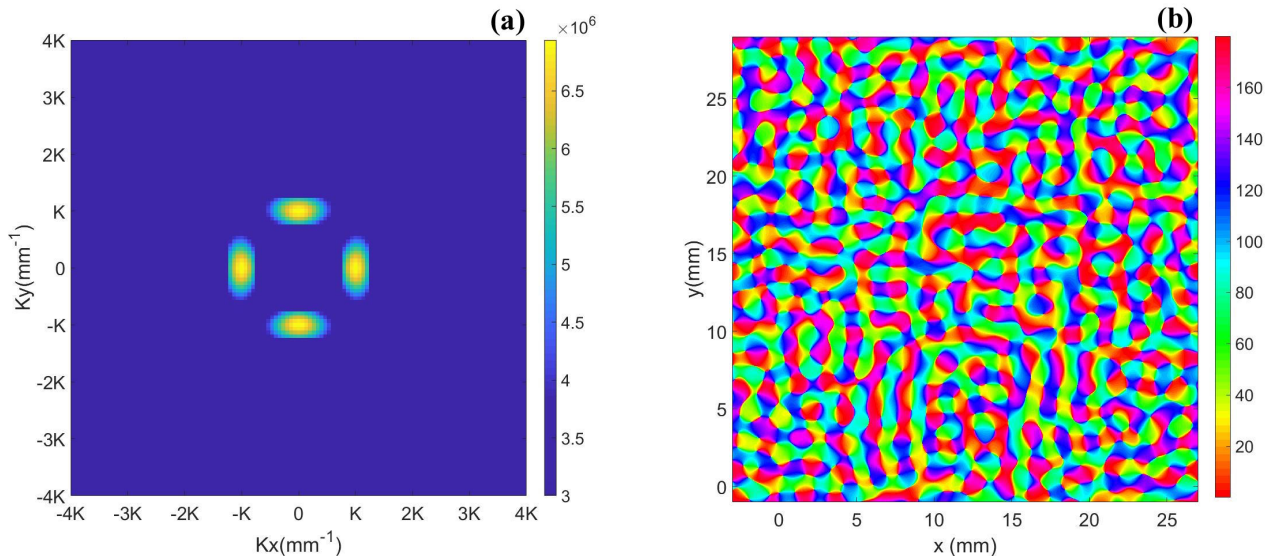


Figure 14: Reconstructed OP-OD map with extra \mathbf{K} in Gaussian envelope. (a) The magnitude plot of \mathbf{K} modes. The color bar indicates the magnitude of it. (b) Reconstructed OP-OD map using set of \mathbf{K} modes shown in (a). The color bar indicates the OP angle in degree.

computational neural network model.

The model of V1 we use here is the Gain Control, Adaptation, Laterally Connected (GCAL) model (Stevens et al., 2013), which treats the retina, LGN, and V1 as 2-dimensional sheets, with neurons in each sheet connected topographically. Neurons not only connect to a small group of neurons of the lower level sheet, but also laterally connect to the neurons within the same sheet. A Hebbian learning rule is adopted in the model for updating the connection weights between neurons (Stevens et al., 2013). Figure 15(a) shows an example output from the GCAL model simulation (Bednar, 2009), and we use this map for further analysis in the Fourier domain.

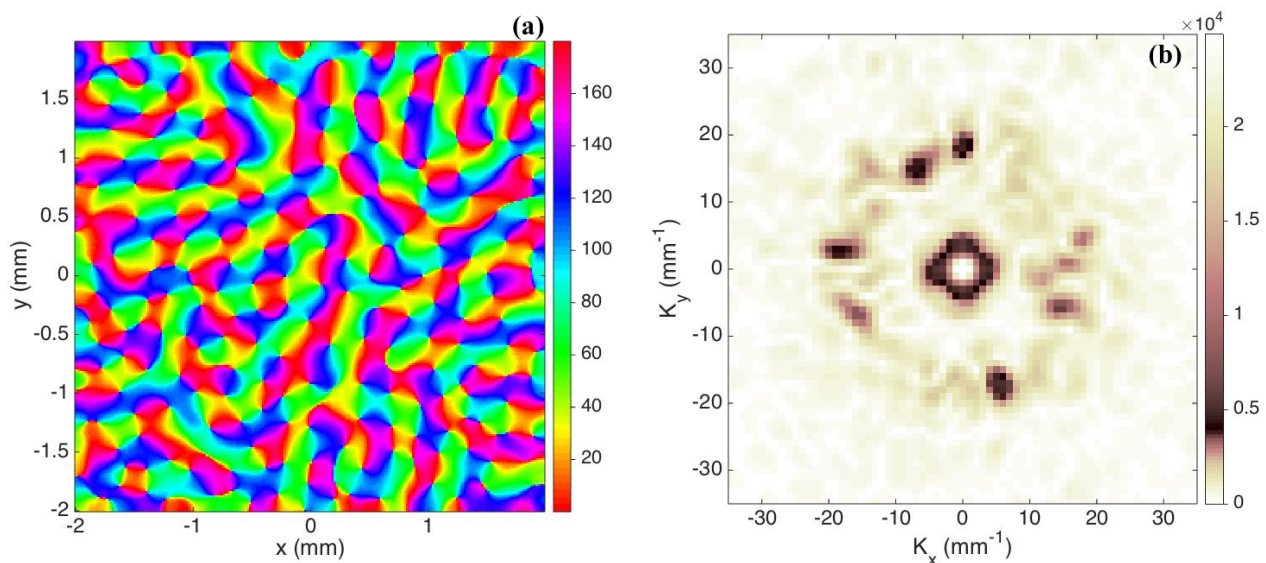


Figure 15: (a) OP map generated from GCAL model (Bednar, 2009), and the color bar indicates the OP angle in degrees. (b) Magnitude plot of the Fourier coefficients obtained from GCAL OP map. Each pixel-like square represents one spatial mode \mathbf{K} , and the color bar indicates its magnitude.

We apply the operator \mathcal{O} to the GCAL OP map and then do a Fourier transform. One thing worth mentioning here is that the OP has discontinuities at the edges of the map if we repeat the whole map in x or y direction, which is implicit in the 2-D discrete Fourier transform. This introduces edge effects

into the Fourier transform, which we minimize by doubling the linear dimensions of the array and zero padding the added region. Figure 15(b) shows the Fourier coefficients after performing Discrete Fourier transform on the zero padded map. The dominant \mathbf{K} terms are shown in black. Except the ring-shaped enhancement near the center, which arises from the zero padding of the map and the linear size of the overall simulation area. The other dominant \mathbf{K} terms correspond to the periodicity of the hypercolumns and have square symmetry similar to the pattern in Fig. 13(a), but with $\sim \pm 15^\circ$ spread of \mathbf{K} . The square symmetry is most likely at least partly due to a combination of: (i) the artifacts introduced by the approximately square OP-OD unit cell, and (ii) a structural bias introduced by the square grid on which the GCAL model is simulated.

6 Summary and Conclusion

In this paper, we present an analytic description of the OP-OD map in V1. It includes modeling both the local neuron sensitivity to the stimulus orientation and the weighted projection from nearby neurons. The results and analysis includes:

(i) we approximate the periodic OP-OD map in a square grid of hypercolumn with parallel left and right OD columns with equal width and OP pinwheels with alternating signs. The approximation is idealized but are good enough for preserving the basic structure of the OP-OD map.

(ii) We propose an AL operator to detect the orientation of the stimulus for local neuron. It is a weighted sum of second order partial derivatives.

(iii) The OP operator reproduces the spatial arrangement of the receptive field of V1 simple cells. It is derived by finding the neuron responses by combining the AL operator with a weighted sum of the projections from neighbouring neurons. We optimize the parameters of the operator by controlling the width and angle selectivity of the response tuning curve, and we find that the orientation tuning is only affected significantly by the aspect ratio of the weight function, not the weights of the second order partial derivatives for detecting input orientation in local neuron. The orientation tuning sharpens when we elongate the OP operator along the orientation axis, in accord with experiment (Hubel and Wiesel, 1962a; Lampl et al., 2001).

(iv) We account for the lower OP sensitivity and lower response strength near pinwheel centers by averaging OP over the characteristic microcolumn scale of $40\ \mu\text{m}$ — near centers many different OPs are averaged together, broadening the tuning curve. A Mexican hat function gives a better match to experiment, raising the possibility of using such experimental results to infer the microscopic connectivity profile.

(v) Fourier domain analysis of the OP-OD maps were performed to generate a set of Fourier coefficients for compact representation and especially for use in NFT. Only the lowest \mathbf{K} modes are needed to described the spatial structure of the hypercolumn. This simplifies the computational work when

we integrate the OP map into the patchy propagator and investigate the neuron activities in V1 using NFT. Moreover, if we keep the lowest \mathbf{K} modes as the basic modes and add extra modes around it using Gaussian envelopes, we could reconstruct a more realistic OP-OD map that is similar to the ones obtained from experiments or computer simulations.

(v) We also perform Fourier analysis on the irregular OP-OD map generated by GCAL model. The dominant \mathbf{K} modes have approximately square symmetry as an artifact of the square grid on which the simulations are done.

Overall, we have succeeded in obtaining compact representations of an idealized joint OP-OD map, in both coordinate and Fourier spaces. Notably, the elongated generalized Gaussian operator dominates in determining OP and mutual consistency OP and OD maps strongly constrains the possible combined maps in hypercolumns, with four pinwheels, not one, required periodic unit of the hypercolumn lattice.

Acknowledgements

This work was supported by the Australian Research Council under Laureate Fellowship grant FL1401000025, Center of Excellence grant CE140100007, and Discovery Project grant DP170101778.

References

- Adams, D. L., Sincich, L. C., and Horton, J. C. (2007). Complete pattern of ocular dominance columns in human primary visual cortex. *J Neurosci*, 27(39):10391–10403.
- Ballard, D. H. and Brown, C. M. (1982). *Computer vision*. Prentice-Hall, Englewood Cliffs, New Jersey.
- Bartfeld, E. and Grinvald, A. (1992). Relationships between orientation-preference pinwheels, cytochrome oxidase blobs, and ocular-dominance columns in primate striate cortex. *Proc Natl Acad Sci USA*, 89:11905–11909.
- Bednar, J. A. (2009). Topographica: Building and analyzing map-level simulations from Python, C/C++, MATLAB, NEST, or NEURON components. *Front Neuroinform*, 3:8.
- Blasdel, G. G. (1992). Orientation selectivity, preference, and continuity in monkey striate cortex. *J Neurosci*, 12:3139–3161.
- Bonhoeffer, T. and Grinvald, A. (1991). Iso-orientation domains in cat visual cortex are arranged in pinwheel-like patterns. *Nature*, 353:429–31.
- Bonhoeffer, T. and Grinvald, A. (1993). The layout of iso-orientation domains in area 18 of cat visual cortex: Optical imaging reveals a pinwheel-like organization. *J Neurosci*, 13:4157–4180.

- Bosking, W. H., Zhang, Y., Schofield, B., and Fitzpatrick, D. (1997). Orientation selectivity and the arrangement of horizontal connections in tree shrew striate cortex. *J Neurosci*, 17(6):2112–2127.
- Bressloff, P. C. and Cowan, J. D. (2002). The visual cortex as a crystal. *Physica D*, 173(3):226–258.
- Chklovskii, D. B. and Koulakov, A. A. (2004). Maps in the brain: What can we learn from them? *Annu Rev Neurosci*, 27:369–392.
- De Valois, R. L. and De Valois, K. K. (1990). *Spatial vision*. Oxford University Press, New York.
- De Valois, R. L., Yund, E. W., and Hepler, N. (1982). The orientation and direction selectivity of cells in macaque visual cortex. *Vision Res*, 22(5):531 – 544.
- DeAngelis, G. C., Ohzawa, I., and Freeman, R. D. (1995). Receptive-field dynamics in the central visual pathways. *Trends Neurosci*, 18(10):451–458.
- Dow, B. M., Snyder, A. Z., Vautin, R. G., and Bauer, R. (1981). Magnification factor and receptive field size in foveal striate cortex of the monkey. *Exp Brain Res*, 44(2):213–228.
- Erwin, E., Obermayer, K., and Schulten, K. (1995). Models of orientation and ocular dominance columns in the visual cortex: A critical comparison. *Neural Comput*, 7:425–468.
- Ferster, D. and Miller, K. D. (2000). Neural mechanisms of orientation selectivity in the visual cortex. *Annu Rev Neurosci*, 23(1):441–471.
- Finn, I. M., Priebe, N. J., and Ferster, D. (2007). The emergence of contrast-invariant orientation tuning in simple cells of cat visual cortex. *Neuron*, 54(1):137–152.
- Gardner, J. L., Anzai, A., Ohzawa, I., and Freeman, R. D. (1999). Linear and nonlinear contributions to orientation tuning of simple cells in the cat’s striate cortex. *Vis Neurosci*, 16(6):1115–1121.
- Graham, N. (1989). *Visual pattern analyzers*, volume 16. Oxford University Press, New York.
- Gur, M., Kagan, I., and Snodderly, D. M. (2005). Orientation and direction selectivity of neurons in V1 of alert monkeys: Functional relationships and laminar distributions. *Cereb Cortex*, 15(8):1207–1221.
- Götz, K. G. (1987). Do “d-blob” and “l-blob” hypercolumns tessellate the monkey visual cortex? *Biol Cybern*, 56(2):107–109.
- Götz, K. G. (1988). Cortical templates for the self-organization of orientation-specific d- and l-hypercolumns in monkeys and cats. *Biol Cybern*, 58(4):213–223.
- Horton, J. C. and Adams, D. L. (2005). The cortical column: A structure without a function. *Philos Trans R Soc Lond B Biol Sci*, 360(1456):837–62.

- Horton, J. C. and Hoyt, W. F. (1991). The representation of the visual field in human striate cortex: A revision of the classic holmes map. *Arch Ophthalmol*, 109(6):816–824.
- Hubel, D. H. and Wiesel, T. N. (1961). Integrative action in the cat’s lateral geniculate body. *J Physiol*, 155(2):385.
- Hubel, D. H. and Wiesel, T. N. (1962a). Receptive fields, binocular interaction and functional architecture in the cat’s visual cortex. *J Physiol*, 160(1):106–154.
- Hubel, D. H. and Wiesel, T. N. (1962b). Shape and arrangement of columns in cat’s striate cortex. *J Physiol*, 165(3):559–568.
- Hubel, D. H. and Wiesel, T. N. (1968). Receptive fields and functional architecture of monkey striate cortex. *J Physiol*, 195(1):215–243.
- Hubel, D. H. and Wiesel, T. N. (1974a). Sequence regularity and geometry of orientation columns in the monkey striate cortex. *J Comp Neurol*, 158(3):267–293.
- Hubel, D. H. and Wiesel, T. N. (1974b). Uniformity of monkey striate cortex: A parallel relationship between field size, scatter, and magnification factor. *J Comp Neurol*, 158(3):295–305.
- Hubel, D. H. and Wiesel, T. N. (1977). Ferrier lecture: Functional architecture of macaque monkey visual cortex. *Proc R Soc Lond B Biol Sci*, 198(1130):1–59.
- Jones, J. P. and Palmer, L. A. (1987). An evaluation of the two-dimensional gabor filter model of simple receptive fields in cat striate cortex. *J Neurophysiol*, 58(6):1233–1258.
- Keliris, G. A., Li, Q., Papanikolaou, A., Logothetis, N. K., and Smirnakis, S. M. (2019). Estimating average single-neuron visual receptive field sizes by fMRI. *Proc Natl Acad Sci U.S.A.*, 116(13):6425–6434.
- Koulakov, A. A. and Chklovskii, D. B. (2001). Orientation preference patterns in mammalian visual cortex: A wire length minimization approach. *Neuron*, 29(2):519–527.
- Lampl, I., Anderson, J. S., Gillespie, D. C., and Ferster, D. (2001). Prediction of orientation selectivity from receptive field architecture in simple cells of cat visual cortex. *Neuron*, 30(1):263–274.
- Liu, X., Sanz-Leon, P., and Robinson, P. A. (2020). Gamma-band correlations in the primary visual cortex. *Phys Rev E*, 101(4):042406.
- Maldonado, P. E., Gödecke, I., Gray, C. M., and Bonhoeffer, T. (1997). Orientation selectivity in pinwheel centers in cat striate cortex. *Science*, 276(5318):1551–1555.

- Mariño, J., Schummers, J., Lyon, D. C., Schwabe, L., Beck, O., Wiesing, P., Obermayer, K., and Sur, M. (2005). Invariant computations in local cortical networks with balanced excitation and inhibition. *Nat Neurosci*, 8(2):194–201.
- Marr, D. (1982). *Vision: A Computational Investigation into the Human Representation and Processing of Visual Information*. W. H. Freeman, San Francisco.
- Marr, D. and Hildreth, E. (1980). Theory of edge detection. *Proc R Soc Lond B Biol Sci*, 207(1167):187–217.
- Marr, D. and Ullman, S. (1981). Directional selectivity and its use in early visual processing. *Proc R Soc Lond B Biol Sci*, 211(1183):151–180.
- Mechler, F. and Ringach, D. L. (2002). On the classification of simple and complex cells. *Vision Res*, 42(8):1017 – 1033.
- Miikkulainen, R., Bednar, J. A., Choe, Y., and Sirosh, J. (2005). *Computational Maps in the Visual Cortex*. Springer-Verlag, New York.
- Mitchison, G. (1991). Neuronal branching patterns and the economy of cortical wiring. *Proc R Soc Lond B Biol Sci*, 245(1313):151–158.
- Mitchison, G. (1995). A type of duality between self-organizing maps and minimal wiring. *Neural Comput*, 7(1):25–35.
- Moore IV, B. D. and Freeman, R. D. (2012). Development of orientation tuning in simple cells of primary visual cortex. *J Physiol*, 107(9):2506–16.
- Movshon, J. A., Thompson, I. D., and Tolhurst, D. J. (1978). Spatial summation in the receptive fields of simple cells in the cat’s striate cortex. *J Physiol*, 283(1):53–77.
- Müller, T. M., Stetter, M., Hübener, M., Sengpiel, F., Bonhoeffer, T., Gödecke, I., Chapman, B., Löwel, S., and Obermayer, K. (2000). An analysis of orientation and ocular dominance patterns in the visual cortex of cats and ferrets. *Neural Comput*, 12(11):2573–2595.
- Nauhaus, I., Benucci, A., Carandini, M., and Ringach, D. L. (2008). Neuronal selectivity and local map structure in visual cortex. *Neuron*, 57(5):673–679.
- Obermayer, K. and Blasdel, G. G. (1993). Geometry of orientation and ocular dominance columns in monkey striate cortex. *J Neurosci*, 13(10):4114–4129.
- Obermayer, K., Blasdel, G. G., and Schulten, K. (1992a). Statistical-mechanical analysis of self-organization and pattern formation during the development of visual maps. *Phys Rev A*, 45(10):7568–7589.

- Obermayer, K., Ritter, H., and Schulten, K. J. (1992b). A model for the development of the spatial structure of retinotopic maps and orientation columns. *IEICE Trans. Fundamentals*, 75(5):537–545.
- Ohki, K., Chung, S., Kara, P., Hübener, M., Bonhoeffer, T., and Reid, R. C. (2006). Highly ordered arrangement of single neurons in orientation pinwheels. *Nature*, 442(7105):925–928.
- Ratliff, F. (1965). *Mach bands: Quantitative studies on neural networks*. Holden-Day, San Francisco.
- Ringach, D. L. (2002). Spatial structure and symmetry of simple-cell receptive fields in macaque primary visual cortex. *J Neurophysiol*, 88(1):455–463.
- Ringach, D. L., Shapley, R. M., and Hawken, M. J. (2002). Orientation selectivity in macaque v1: Diversity and laminar dependence. *J Neurosci*, 22(13):5639–5651.
- Robinson, P. A. (2005). Propagator theory of brain dynamics. *Phys Rev E*, 72:011904.
- Robinson, P. A. (2006). Patchy propagators, brain dynamics, and the generation of spatially structured gamma oscillations. *Phys Rev E*, 73:041904.
- Robinson, P. A. (2007). Visual gamma oscillations: Waves, correlations, and other phenomena, including comparison with experimental data. *Biol Cybern*, 97:317–335.
- Schiller, P. H. and Tehovnik, E. J. (2015). *Vision and the Visual System*. Oxford University Press, Oxford.
- Schummers, J., Mariño, J., and Sur, M. (2002). Synaptic integration by v1 neurons depends on location within the orientation map. *Neuron*, 36(5):969–978.
- Skottun, B. C., De Valois, R. L., Grosof, D. H., Movshon, J. A., Albrecht, D. G., and Bonds, A. (1991). Classifying simple and complex cells on the basis of response modulation. *Vision Res*, 31(7-8):1078–1086.
- Smith, A. T., Singh, K. D., Williams, A. L., and Greenlee, M. W. (2001). Estimating receptive field size from fMRI data in human striate and extrastriate visual cortex. *Cereb Cortex*, 11(12):1182–1190.
- Stevens, J. R., Law, J. S., Antolík, J., and Bednar, J. A. (2013). Mechanisms for stable, robust, and adaptive development of orientation maps in the primary visual cortex. *J Neurosci*, 33(40):15747–15766.
- Swindale, N. V. (1992). A model for the coordinated development of columnar systems in primate striate cortex. *Biol Cybern*, 66(3):217–230.
- Swindale, N. V. (1996). The development of topography in the visual cortex: A review of models. *Network*, 7(1):161–247.

- Swindale, N. V. (1998). Orientation tuning curves: Empirical description and estimation of parameters. *Biol Cybern*, 78(1):45–56.
- Swindale, N. V., Grinvald, A., and Shmuel, A. (2003). The spatial pattern of response magnitude and selectivity for orientation and direction in cat visual cortex. *Cereb Cortex*, 13(3):225–238.
- Tootell, R. B. H., Silverman, M. S., Switkes, E., and De Valois, R. L. (1982). Deoxyglucose analysis of retinotopic organization in primate striate cortex. *Science*, 218(4575):902–904.
- Torre, V. and Poggio, T. A. (1986). On edge detection. *IEEE Trans Pattern Anal Mach Intell*, (2):147–163.
- Toth, L. J., Kim, D. S., Rao, S. C., and Sur, M. (1997). Integration of local inputs in visual cortex. *Cereb Cortex*, 7(8):703–710.
- Tovée, M. J. (1996). *An Introduction to the Visual System*. Cambridge University Press, Cambridge.
- Troyer, T. W., Krukowski, A. E., Priebe, N. J., and Miller, K. D. (1998). Contrast-invariant orientation tuning in cat visual cortex: Thalamocortical input tuning and correlation-based intracortical connectivity. *J Neurosci*, 18(15):5908–5927.
- Veltz, R., Chossat, P., and Faugeras, O. (2015). On the effects on cortical spontaneous activity of the symmetries of the network of pinwheels in visual area V1. *J Math Neurosci*, 5(1):11.
- Yacoub, E., Harel, N., and Uğurbil, K. (2008). High-field fMRI unveils orientation columns in humans. *Proc Natl Acad Sci USA*, 105(30):10607–10612.
- Young, R. A. (1987). The gaussian derivative model for spatial vision: I. Retinal mechanisms. *Spat Vis*, 2(4):273–293.
- Young, R. A., Lesperance, R., and Meyer, W. W. (2001). The gaussian derivative model for spatial-temporal vision: I. Cortical model. *Spat Vis*, 14(3-4):261–319.